Array 28 (2025) 100535

Contents lists available at ScienceDirect

Array

journal homepage: www.elsevier.com/locate/array

Multi-scale signal-to-noise driven fusion of post-processing sequences for enhanced defect detectability in active infrared thermography

R. Usamentiaga [a,*], S. Sfarra [b], C. Ibarra-Castanedo [c], H. Zhang [c], X. Maldague [c]

[a] Department of Computer Engineering, University of Oviedo, Campus de Viesques, 33204 Gijón, Spain
[b] Department of Industrial and Information Engineering and Economics (DIIIE), University of L'Aquila, L'Aquila, I-67100, Italy
[c] Department of Electrical and Computer Engineering, Computer Vision and Systems Laboratory (CVSL), Laval University, Quebec, G1V 0A6, Canada

ARTICLE INFO

Keywords:
Active infrared thermography
Multi-sequence fusion
Defect detection
Signal-to- noise ratio
Non-destructive testing

ABSTRACT

Active infrared thermography has emerged as a crucial tool in non-destructive testing, providing real-time visual representations of thermal patterns on material surfaces. However, detecting and analyzing defects can be challenging due to noise interference, the lack of standardization in post-processing techniques, complexity in data analysis, variability in defect visibility across frames, and the influence of environmental factors. To address these limitations, this study proposes a novel approach that enhances defect detectability by fusing multiple sequences derived from various post-processing methods into single, interpretable images. The proposed approach employs a multi-scale signal-to-noise ratio metric to accurately identify regions of interest and determine the optimal time at which defect detectability is maximized. Validation with two composite specimens featuring diverse defect characteristics demonstrates the capability of the method to simplify analysis and reliably improve detection performance. Compared with wavelet-based image fusion, the proposed approach achieves superior defect visibility and clarity, demonstrating a significant advancement in the effectiveness and reliability of thermographic inspections.

1. Introduction

Inspection methods using infrared thermography (IRT) have proven to be an invaluable tool across a wide range of applications [1,2], including electrical and mechanical inspections [3], monitoring equipment [4], identification of insulation deficiencies [5], medical and veterinary [6] or wildfire detection [7] among many others [8,9]. In particular, active IRT has established itself as one of the most popular techniques in the field of non-destructive testing (NDT) [10,11], which refers to a set of inspection techniques used to evaluate the properties, integrity, and condition of materials, components, or structures without causing any damage or altering their usefulness. This popularity can be attributed to several advantages it offers over traditional methods, such as X-ray and ultrasonic testing. One significant advantage of active IRT is its ability to provide real-time, visual representations of thermal patterns on the surface of materials, enabling quick identification of defects such as cracks, delaminations, and voids [12]. Unlike X-ray methods, which require careful handling and safety precautions due to radiation exposure, IRT is non-invasive and safe for both operators and the environment. Additionally, it allows for the inspection of larger areas in a shorter amount of time, making it highly efficient for industrial applications [13].

Active infrared thermography works by inducing excitation in the material, typically through the application of heat [11]. This heating creates a thermal response in the material, which is then monitored using an infrared camera, as can be seen in Fig. 1. The thermal system captures the emitted infrared radiation, producing a sequence of infrared images that reflect the temperature distribution across the surface of the inspected object over time [14]. The key principle behind this method is that different materials and defects will exhibit varying thermal responses due to differences in thermal conductivity, heat capacity, and density. Defects such as cracks, voids, or delaminations often lead to anomalies in the thermal profile, which can be detected as variations in temperature over time [15,16]. Active IRT can be employed in a variety of settings, from aerospace to civil engineering, demonstrating its versatility. By using controlled heating to induce temperature differentials in materials, this technique enhances defect detectability, providing detailed information that can inform maintenance and repair decisions. As a result, active IRT not only enhances safety and quality assurance but also contributes to the overall efficiency and reliability of industrial processes [2].

Despite the success of IRT in many NDT applications, it still faces challenges that can limit its effectiveness. One significant issue is

* Corresponding author.
E-mail address: rusamentiaga@uniovi.es (R. Usamentiaga).

https://doi.org/10.1016/j.array.2025.100535
Received 21 July 2025; Received in revised form 10 October 2025; Accepted 10 October 2025
Available online 15 October 2025

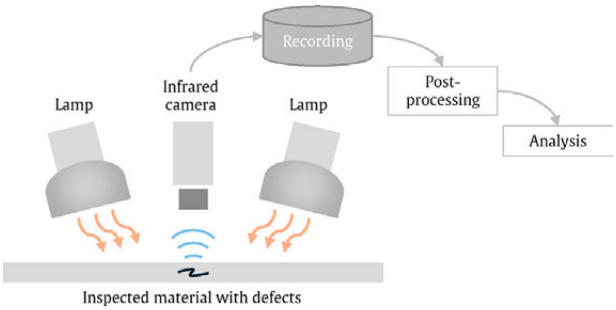

Fig. 1. Active infrared thermography in non-destructive testing.

the detection of subtle subsurface anomalies, which often produce weak thermal signals that can be obscured by noise in the thermographic data. This noise can hinder accurate visual inspection and lead to missed defects, compromising the reliability of the inspection process. Moreover, factors such as environmental conditions and material properties can further complicate the interpretation of thermal images. For instance, variations in surface emissivity, background temperature fluctuations, and atmospheric conditions can all affect the thermal response, making it difficult to discern meaningful data from the noise [17]. To mitigate these challenges, researchers and practitioners increasingly rely on post-processing techniques that enhance the signal-to-noise ratio of the acquired thermographic data. Techniques such as statistical moments [18], Fourier transform analysis [19], Principal Component Analysis [20] and Thermographic Signal Reconstruction (TSR) [21] are commonly employed to optimize the detection and visualization of defects, leading to improved identification rates and more reliable assessments.

Several significant challenges impact the effectiveness of post-processing techniques in NDT. First, there is a lack of consensus within the NDT community regarding the most appropriate post-processing methods for specific materials and defect types. While some general recommendations exist, many practitioners often rely on a trial-and-error approach to determine the best method for their particular applications [22]. Moreover, most post-processing techniques generate a new sequence of thermal images that must be meticulously analyzed to identify the presence of defects. This additional layer of complexity can complicate the inspection process, as operators must carefully review the processed data to ensure that no anomalies are overlooked. For example, when applying Principal Component Analysis (PCA) in NDT for detecting voids or delaminations in carbon fiber, it is often observed that the fourth component yields the clearest visualization of these defects [23]. In contrast, when IRT is utilized for inspecting cultural heritage using solar loading, the most relevant component for anomaly detection can be significantly higher, sometimes reaching the 10th component or even beyond [24]. Without prior knowledge of these patterns, technicians are compelled to analyze multiple images to conduct a thorough inspection and analysis, which can be time-consuming and may lead to missed defects. This highlights the importance of developing standardized methodologies and frameworks that can guide practitioners, for example, in selecting the appropriate components for specific applications, thereby improving the efficiency and accuracy of inspections in both industrial and cultural contexts.

The visibility of defects in the infrared sequence or in the resulting post-processed images depends on several factors, including the characteristics of the defects, the materials being analyzed, their depth, and even environmental conditions. Consequently, some defects may reach maximum contrast in one frame, while others may be best visualized in a different frame. This variability means that there is no single frame in which all defects are optimally visualized, making the interpretation of results significantly more challenging. An example of this challenge can be seen in NDT applied to carbon fiber materials, where the visibility of defects in the thermal images varies based on the depth of the defect. Specifically, the frame in which a defect is most clearly visible is influenced by its depth within the material. For deeper defects, the frame that provides the best visualization typically occurs significantly later in the thermal sequence, often many images after the initial excitation. This delay in optimal visualization contrasts sharply with shallow defects, which can be identified close to the moment of excitation. The differences in optimal timing are attributed to the varying thermal response of materials, as deeper defects may require additional time for thermal diffusion to reveal their presence clearly. This variability complicates the analysis process, as technicians must analyze multiple images over a longer timeframe to accurately assess the condition of the material. The challenge highlights the necessity for advanced methods that can integrate and present the information from these sequences in a more manageable format.

To address the limitations of current post-processing practices in active infrared thermography (IRT) for non-destructive testing (NDT), this study proposes a novel fusion-based methodology that integrates multiple post-processed thermal sequences into single, information-rich images. Traditional approaches often require technicians to manually inspect large sets of frames or components from various post-processing techniques, each emphasizing different thermal features depending on defect characteristics, depth, and material properties. This trial-and-error process is time-consuming and error-prone, especially in applications where the optimal frame for defect visibility varies significantly. Our method mitigates this issue by employing a Multi-Sequence Contrast-to-Noise Ratio (MS-CNR) metric to automatically identify regions and frames of interest across different sequences. It then fuses this information into four condensed visual representations (Maxigram, Sigmagram, Timegram, and Sourcegram) that preserve and highlight the most diagnostically relevant thermal features.

Alternative image fusion wavelet-based fusion [25] has been employed to combine images from different processing methods, preserving edge resolution and accurately representing defect shapes. This is typically performed using a three-level wavelet decomposition, applying maximum selection for approximations and minimum selection for details, resulting in a single fused image that integrates the complementary information from phase analysis and PCA. In contrast, the proposed approach extends this concept by fusing multiple sequences using the MS-CNR metric, enabling automatic identification of optimal frames and regions, and producing condensed visual representations that further improve defect visibility and clarity.

By integrating complementary information from multiple post-processing techniques, our approach enhances the interpretability, reliability, and automation of defect detection. It simplifies the decision-making process for operators, reducing the cognitive burden and increasing the efficiency of inspections across a wide range of applications. Importantly, the proposed framework is agnostic to the type of defect or excitation method, making it broadly applicable and scalable. In doing so, this work directly addresses key research gaps related to standardization, interpretability, and automation in IRT-based NDT, offering a powerful tool for improving the clarity, accuracy, and practical utility of thermal inspections.

The theoretical analysis of the proposed method can be interpreted through the physical principles of active infrared thermography. When an external thermal excitation is applied, heat propagates through the material according to its thermal properties, and defects such as delaminations or voids locally alter this heat flow, creating characteristic thermal contrasts on the surface. The proposed fusion and post-processing techniques enhance these contrasts by emphasizing temporal and spatial variations in the thermal response, which correspond directly to the underlying heat diffusion dynamics and defect-induced perturbations. By modeling the expected thermal decay and its interaction with subsurface anomalies, the method can be theoretically justified not only as a signal-processing enhancement but also as a

physically grounded approach that amplifies the signatures of real defects in accordance with thermodynamic principles.

Recent advancements in quality control have been driven by non-destructive testing methods [26], particularly leveraging deep learning techniques [27]. Prior research has delved into object detection [28–30], semantic segmentation [31], and innovative hybrid approaches that integrate both methods using the Segment Anything Model (SAM) [23,32]. Additionally, deep learning has been used to overcome the resolution limitations inherent in infrared imaging [33,34], enabling the enhancement of image quality and the improved detection of subtle defects. These advancements in deep learning-driven NDT approaches are opening new possibilities for more accurate and efficient quality control in various industrial applications. Despite these strides, post-processing techniques remain indispensable in non-destructive testing workflows. Automated defect detection is still evolving, with its accuracy and robustness largely dependent on access to extensive, high-quality datasets. The approach proposed here is designed to complement and enhance these existing methodologies.

This paper is structured as follows: Section 2 reviews the existing post-processing methods; Section 3 describes the proposed approach; Section 4 presents the results from real data in infrared non-destructive inspection, and finally, Section 5 provides the concluding remarks.

2. Post-processing methods in active thermography

In active IRT, post-processing methods play a critical role in enhancing defect detectability [35,36]. These techniques involve the analysis of thermal data captured during the inspection process, focusing on improving signal-to-noise ratios, enhancing contrast, and isolating defect signatures from background thermal variations [37,38]. By refining the raw thermal data, post-processing techniques enable more accurate identification of defects, particularly those that are subtle or difficult to detect using initial imaging alone.

In the context of active IRT, post-processing techniques can be broadly divided into two categories based on their output: methods that produce a sequence of images and those that generate a single image. Despite this difference in output, both types of methods work from the same input—thermal data captured during and after the heat excitation, typically in the form of an infrared video. This video contains the thermal responses of the material to the applied stimulus.

Methods that produce a single image offer the advantage of simpler analysis, as they condense the thermal information into one frame that highlights potential defects or anomalies. However, this simplification often comes at the cost of a worse signal-to-noise ratio, as key temporal or frequency-based information is lost during compression of the data into a single output. Examples of these methods include Skewness, Kurtosis [18] or, more recently, MSGSA [39].

On the other hand, methods that produce a sequence of images retain more of the underlying data, allowing for richer analysis by preserving temporal or frequency variations in the thermal response. These methods generally provide better defect detection and characterization due to their ability to isolate and emphasize defect-related features across multiple frames, but they often require more complex and time-consuming analysis.

Other types of classifications for post-processing techniques in active infrared thermography have been proposed, including those based on thermal contrast, signal transforms, and statistical analysis methods [40]. Thermal contrast techniques aim to enhance defect visibility by emphasizing temperature differences over time. For example, Local Boundary Contrast is a method designed to enhance defect visibility by emphasizing local variations in temperature [41,42]. It evaluates the difference between the temperature at a central spot and the average temperature of its surrounding area. Ideally, non-defective regions should yield near-zero contrast, while defects produce noticeable differences due to their anomalous thermal behavior. This method improves defect boundary visualization, especially in challenging conditions such as non-uniform heating or pre-heating accumulation, and supports better shape reconstruction of subsurface flaws. On the other hand, statistical methods leverage statistical descriptors to characterize and enhance subtle thermal patterns associated with subsurface defects.

Over the past few decades, a wide range of these methods have been proposed. Below, a brief introduction to some of the most commonly used techniques is provided, highlighting their unique features and applications.

2.1. Thermography Signal Reconstruction (TSR)

In this method, the temperature–time profile of each pixel in the thermal sequence is approximated using a polynomial fit, commonly referred to as Thermographic Signal Reconstruction (TSR) [21]. The temperature evolution is modeled by fitting an n-degree polynomial, as shown in (1).

$$T(t) = a_n t^n + a_{n-1} t^{n-1} + \cdots + a_1 t + a_0 \tag{1}$$

In pulse thermography, the method typically requires transforming the signals into the logarithmic domain prior to processing to linearize the thermal response and enhance defect visibility. In contrast, for step heating thermography, such a transformation is not necessary [43], as the gradual heating allows thermal contrasts to develop naturally over time. Despite this, TSR has been successfully applied to step thermography, where it effectively reduces noise and improves defect detectability. In many cases, TSR serves as a valuable pre-processing step that enhances the performance of subsequent post-processing methods, making it a meaningful and practical tool even in step heating scenarios.

Polynomial fitting provides the ability to filter noise and compress the thermal sequence, as only the polynomial coefficients are needed for sequence reconstruction. Furthermore, it enables the analytical computation of time derivatives, which have been demonstrated to significantly improve defect visualization, especially when using the second derivative [22].

One disadvantage of this approach is that the frame in which the maximum signal-to-noise ratio is achieved for a given defect depends on its depth. As a result, the optimal frame for detecting one defect may differ significantly from the best frame for detecting another. This variability complicates the analysis, as it requires careful selection of frames to ensure that defects at different depths are properly visualized.

2.2. Principal Component Thermography (PCT)

Principal Component Thermography (PCT) leverages PCA, a statistical technique aimed at synthesizing information by reducing the number of variables in a dataset while retaining as much relevant information as possible. In the context of active IRT, PCT helps streamline large amounts of thermal data, focusing on key features that enhance defect detection.

The core of PCT lies in Singular Value Decomposition (SVD), which decomposes the thermal sequence into a set of statistically orthogonal functions known as Empirical Orthogonal Functions (EOF) [20]. These EOFs represent different modes of variation in the thermal data, with the first few components capturing the most significant information. The initial components retain most of the thermal response related to defects while reducing noise and irrelevant data.

By reducing the dataset to these principal components, PCT simplifies the analysis, allowing users to focus on a reduced number of frames without sacrificing critical defect information. This makes it particularly effective for enhancing the visibility of defects in complex thermal image sequences where the raw data may contain substantial noise or irrelevant variations. Moreover, this method improves the signal-to-noise ratio, enabling clearer identification of subsurface defects that might otherwise be obscured.

A key strength of PCT is its ability to highlight subtle thermal anomalies that may not be immediately visible in raw or unprocessed thermographic data. By emphasizing the most relevant thermal variations, it aids in distinguishing between defect-related features and background noise. However, like any dimensionality reduction technique, there is a potential trade-off: as more components are discarded, some level of detail may be lost, potentially overlooking very fine or deep defects. Therefore, careful selection of components is critical to ensuring optimal results.

Although the first few components in PCT typically capture the most significant information related to defects, there are specific scenarios where components of greater order become essential. One notable example is in cases of solar loading in cultural heritage applications. In such contexts, thermal responses can be influenced by varying surface conditions and external environmental factors, making it crucial to examine higher-order components to fully understand the thermal behavior of the materials. For example, in [44], it was demonstrated that component 36 exhibited the greatest variation in temperature, underscoring the importance of analyzing higher-order components in specific scenarios. This finding highlights that, in certain contexts, such as the thermal assessment of cultural heritage structures, the most relevant information regarding temperature variations may reside in components that are not traditionally prioritized.

2.3. Pulse Phase Thermography (PPT)

Pulsed Phase Thermography (PPT) relies on the application of the Fast Fourier Transform (FFT) to the temperature–time history of each pixel in the acquired thermographic sequence. This method approximates the temperature–time profile as a sum of harmonic waves at various frequencies, thus capturing the frequency response of the thermal stimulus. The calculation is performed according to (2), where i represents the imaginary unit, n indicates the frequency increment, and Re_n and Im_n denote the real and imaginary components of the Discrete Fourier Transform (DFT).

$$F_n = \sum_{k=1}^{N-1} T(k)\, e^{\frac{2\pi i k n}{N}} = Re_n + Im_n \tag{2}$$

The phase information derived from this process is particularly important, as it reveals significant details about the material's structural properties. This phase can be calculated using (3).

$$\emptyset_n = \operatorname{atan}\left(\frac{Im_n}{Re_n}\right) \tag{3}$$

This method was initially proposed for pulse thermography [19,45], but it is also applicable to step heating inspections.

2.4. Partial least square thermography (PLST)

Partial Least Squares Thermography (PLST) is grounded in statistical correlation, aimed at optimizing infrared inspection processes. This method decomposes the temperature–time history into a set of latent variables through the use of partial least squares regression. By focusing on the relationship between the input data (the temperature–time history) and the output (the presence of defects), PLST effectively identifies the underlying patterns that are most relevant for defect detection.

In this approach, irrelevant information is systematically discarded, ensuring that only the most significant data is utilized in the regression analysis. This selective retention enhances the accuracy of the model by reducing noise and emphasizing critical thermal responses related to defects. Additionally, PLST addresses the challenges posed by non-uniform heating, a common issue in thermographic inspections, by removing its effects while maintaining physical consistency in the analysis [46].

The strength of PLST lies in its ability to integrate multiple temperature–time profiles and their correlations into a unified model, allowing for a more comprehensive understanding of the thermal behavior of materials. This capability not only improves the detection of defects but also enhances the reliability of the inspection results.

2.5. Other methods

The reviewed methods represent the most commonly used approaches to process thermal sequences in active thermography. However, in recent years, a wide array of advanced methods and excitation techniques have been proposed, aiming to overcome some of the limitations of conventional approaches, particularly regarding noise suppression, resolution enhancement, and adaptability to complex inspection scenarios. A few representative examples are briefly summarized below.

A defect super-resolution algorithm based on infrared thermal imaging physical kernels was introduced in [47]. This method incorporates the modulation transfer function of the infrared system as a physical prior to reconstruct degraded thermal images. To deal with large and irregularly shaped samples, an automated thermography cognitive sensing–feedback framework has been proposed [48]. This method integrates robotic inspection with thermal perception, using a heat flux density isobaric surface projection as a physical constraint. Advanced matrix and tensor decomposition methods have also gained traction. For example, a differentiate tensor low-rank soft decomposition technique has been developed to extract weak defect information from noisy thermal patterns [49]. This approach leverages probabilistic tensor models and Tucker decomposition to enhance defect contrast, suppress interference such as light spots, and improve robustness in complex composite inspections. Similarly, ensemble joint sparse low-rank matrix decomposition has been proposed for thermography-based diagnosis [50]. By jointly modeling low-rank and sparse structures in thermal data, this method enhances the separation of weak defect signals from strong background noise, achieving superior contrast and lower computational cost compared to conventional low-rank decomposition approaches. Together, these methods illustrate how the field is increasingly adopting concepts from signal processing, statistical learning, and robotic automation to push the boundaries of active thermography, providing more robust, adaptive, and high-resolution defect detection.

It is worth noting that the proposed multi-sequence fusion approach is not constrained to any specific post-processing method or excitation technology. On the contrary, it is inherently flexible and can integrate sequences or images derived from different techniques, whether traditional (e.g., TSR, PCT, PPT, PLST) or more recent methods such as super-resolution, tensor decomposition, or sparse low-rank modeling. By condensing complementary information from multiple sources into cohesive images, the approach enables a more comprehensive representation of defect signatures. This flexibility ensures that diverse post-processing outputs can be effectively combined, yielding concise yet informative images that simplify interpretation while preserving enhanced defect visibility.

3. Proposed approach

3.1. Overall approach

The proposed approach integrates multiple sequences derived from various post-processing techniques, such as those previously discussed, to generate single images that enhance the identification of defects or anomalies. To achieve multi-sequence fusion, a multi-scale contrast-to-noise ratio (MS−CNR) metric is employed. This metric helps identify regions of interest within the images and determines the optimal timing for maximizing defect detectability.

The overall process flow is summarized in Fig. 2, which also serves as a graphical abstract of the methodology, providing a concise visual representation of the fusion framework. The raw infrared sequence, which captures the thermal responses of the material to the applied stimulus, undergoes analysis through various post-processing techniques. The results from these techniques are subsequently merged into a single sequence by concatenating them. Following this, the MS−CNR metric is applied to generate different images that condense the analyzed information:

- Maxigram: an image that contains the maximum contrast achieved for each pixel using the MS−CNR metric. This provides a comprehensive visualization of the highest contrast across the image.
- Sigmagram: an image that represents the scale, indicated by the sigma values at which the maximum contrast is achieved. This captures the scale at which the maximum contrast is achieved, indicated by the specific sigma values. This is crucial for understanding the spatial level of detail where defects are most prominent.
- Sourcegram: an image that contains the normalized source value corresponding to where the maximum contrast is achieved. This offers a deeper connection between the contrast and its originating intensity.
- Timegram: an image that indicates the frame number at which the maximum contrast is achieved. This is particularly relevant in dynamic or time-dependent imaging scenarios.

The four grams, maxigram, sigmagram, sourcegram, and timegram, are selected because they represent complementary strategies for capturing different aspects of defect visibility over time and across spatial scales. These methods show strong performance and provide a good balance between robustness and computational efficiency. However, other contrast-based strategies, such as maximum intensity minus the median or mean (i.e., max-median or max-mean), could be valuable additions. In fact, integrating such methods as a fifth or additional technique is entirely feasible within the proposed framework, which is modular by design and can accommodate other metrics or representations that may be better suited for specific defect types.

To preserve the information from different post-processing techniques, the resulting sequences are concatenated along the frame dimension, without applying any additional transformations. Each post-processing technique produces a sequence of images (a 3D tensor with dimensions corresponding to height, width, and frame). By concatenating these sequences, we form a single, longer 3D tensor that integrates all post-processing results. The proposed approach then analyzes this combined tensor at multiple spatial scales, selecting, for each pixel, the frame that provides the highest contrast according to the MS−CNR metric. This strategy ensures that information from all post-processing sequences is retained and can contribute to enhanced defect detection.

The concepts of Maxigram and Timegram are also introduced in Dynamic Thermal Tomography (DTT) [51]. However, in DTT, the Maxigram is calculated by assessing the contrast over time using higher-order polynomials, resulting in a fundamentally different approach [52]. This distinction highlights the unique nature of our method, which integrates multi-sequence analysis and multi-scale techniques to capture a broader range of defect characteristics across spatial and temporal domains.

3.2. MS−CNR *metric*

The MS−CNR is a metric designed to evaluate contrast without the need for explicit definitions of defective and sound areas [53]. It accomplishes this by applying the Laplacian of Gaussian (LoG) operator, an extension of the basic Laplacian operator, to the image at multiple scales. These scales are determined by the standard deviation

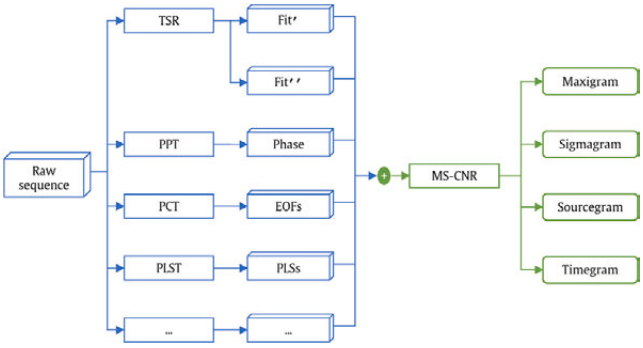

Fig. 2. Flowchart of the proposed method.

of the Gaussian function, allowing the MS−CNR to effectively capture contrast variations across a range of spatial frequencies. The overall contrast is computed as the maximum normalized response derived from these different scales.

The LoG is a second-order differential equation with profound implications in various fields of mathematics and physics, with significant applications in image processing, signal processing, and fluid dynamics. Notably, it has been employed extensively to detect local maxima or blobs within images at specific scales, as in [54]. Recent applications also include defect detection in infrared images [55].

In mathematical terms, the Laplacian operator is formally defined as the spatial derivative of the gradient of a function. This operational framework enables the quantification of spatial deviations from a local average value, thereby providing insight into the underlying structure and topology of a given function or image domain.

In the context of image processing, the Laplacian of an image I can be explicitly expressed as (4).

$$\nabla^2 I = \frac{\partial^2 I}{\partial x^2} + \frac{\partial^2 I}{\partial y^2} \tag{4}$$

The LoG operator is a refined variant of the classical Laplacian operator that leverages the benefits of Gaussian smoothing to augment its capabilities in image processing applications. By incorporating a Gaussian filter into the traditional Laplacian framework, the LoG operator reduces the effects of noise while maintaining its ability to highlight regions of rapid intensity change, thereby facilitating feature identification in noisy image data.

Mathematically, the LoG operator can be expressed as (5), where n_{σ_x,σ_y} is a Gaussian function defined by (6). In this expression, σ_x and σ_y are the standard deviations in the x and y directions, respectively.

$$\nabla^2 n_{\sigma_x,\sigma_y}(x,y) = \frac{\partial^2}{\partial x^2}(n_{\sigma_x,\sigma_y}) + \frac{\partial^2}{\partial y^2}(n_{\sigma_x,\sigma_y}) \tag{5}$$

$$n_{\sigma_x,\sigma_y}(x,y) = \frac{1}{2\pi\sigma_x\sigma_y}\exp\left(-\frac{x^2}{2\sigma_x^2} - \frac{y^2}{2\sigma_y^2}\right) \tag{6}$$

Combining both expressions, the Laplacian of Gaussian can then be defined using (7). Fig. 3 shows the graphical representation of the operator.

$$\nabla^2 n_{\sigma_x,\sigma_y}(x,y) = \frac{1}{\pi\sigma_x^2\sigma_y^2}\left[\frac{x^2}{\sigma_x^4} + \frac{y^2}{\sigma_y^4} - \frac{1}{\sigma_x^2} - \frac{1}{\sigma_y^2}\right] \exp\left(-\frac{x^2}{2\sigma_x^2} - \frac{y^2}{2\sigma_y^2}\right) \tag{7}$$

The Laplacian of Gaussian can then be defined using (8). The parameters σ_x and σ_y play a crucial role in shaping the behavior of the LoG operator, as they control the extent of smoothing in the x and y directions, respectively. By varying these parameters, it is possible to trade-off between noise reduction and sensitivity to fine details,

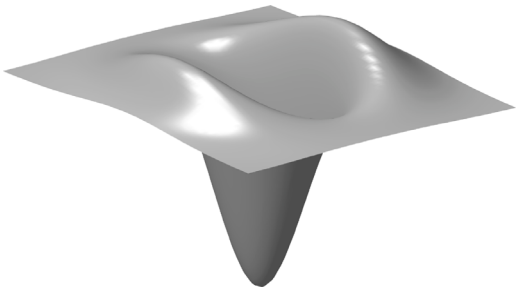

Fig. 3. Laplacian of Gaussian (LoG) operator ($\sigma_x = 10$ and $\sigma_y = 15$).

allowing for the detection of features at different scales. Larger values of σ_x and σ_y result in increased smoothing, which tends to suppress finer details and reduce the operator's ability to detect noise, while smaller values tend to preserve more detail and enhance the operator's sensitivity to small-scale structures.

$$\nabla^2 n_{\sigma_x,\sigma_y}(x,y) = \frac{1}{\pi\sigma_x^2\sigma_y^2}\left[\frac{x^2}{\sigma_x^4}+\frac{y^2}{\sigma_y^4}-\frac{1}{\sigma_x^2}-\frac{1}{\sigma_y^2}\right] \exp\left(-\frac{x^2}{2\sigma_x^2}-\frac{y^2}{2\sigma_y^2}\right) \tag{8}$$

The formulation of the LoG operator has been complemented by various parameterizations that incorporate rotational symmetry, allowing for more effective detection of features in varying orientations [56]. These extensions, however, introduce a significant computational burden when it comes to optimizing the operator's performance.

The MS−CNR exploits the multi-scale feature detection capability of the Laplacian of Gaussian (LoG) operator to evaluate contrast at different spatial levels. This approach enables the MS−CNR to analyze contrast variations occurring at both fine and coarse levels of detail. By convolving the image I with the LoG operator using different values of σ_x and σ_y, the MS−CNR captures contrast changes across a range of scales. This process ensures that contrast differences are effectively quantified in objects of varying sizes. For instance, in the case of narrow defects such as cracks, selecting a high σ_x and a low σ_y allows the metric to better capture the anisotropic contrast between the defect and the surrounding sound area. This directional sensitivity enhances the detection of elongated or narrow features that may otherwise be suppressed when using isotropic filtering, thus improving the robustness of defect characterization across diverse scenarios.

The MS−CNR formulation in Eq. (9) applies the Laplacian of Gaussian (LoG) operator at multiple spatial scales to extract thermal contrast across different levels of detail. At each scale, the response is normalized by a local estimate of the noise level, resulting in a scale-specific contrast-to-noise ratio. The use of the absolute value of the convolution ensures that both positive and negative contrast variations are captured, providing a comprehensive representation of intensity changes. This multi-scale approach allows the metric to robustly highlight both fine and coarse features, making it well-suited for complex image structures.

$$\text{MS−CNR}(I) = \max_{(x,y,\sigma_x,\sigma_y)} \frac{\left|\sigma_x\sigma_y\nabla^2 n_{\sigma_x,\sigma_y} * I(x,y)\right|}{\sigma_N} \tag{9}$$

To maintain consistency when applying the LoG operator across different scales, the operator is scaled by the product of the standard deviations σ_x and σ_y in the x and y directions. This adjustment ensures that the LoG response remains uniform, regardless of scale, and accounts for any directional differences in smoothing, preventing anisotropic effects. This normalization effectively compensates for the differences in response caused by variations in the standard deviations. However, it does not account for differences in intensity scales between images. To address this, the MS−CNR introduces a second normalization step that takes into consideration the background noise σ_N, ensuring consistent contrast evaluation across images with varying intensity levels.

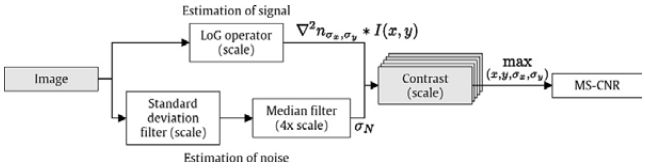

Fig. 4. Active infrared thermography in non-destructive testing.

The proposed method for estimating noise, denoted as σ_N in (9), is based on standard deviation filtering within the neighborhood defined by the LoG operator at each scale. This approach enables dynamic noise estimation that is scale-sensitive, ensuring an accurate contrast-to-noise ratio evaluation. The filtering is applied to a neighborhood where the LoG operator's response is positive (see Fig. 3), and the noise level σ_N is calculated as the median of the standard deviation within the region. This method provides a robust estimate of noise by considering variability across a sufficiently large area, capturing both the signal (defect region) and surrounding noise (sound area). The use of the median minimizes the influence of outliers, such as edges where standard deviation is typically much higher than the noise, ensuring reliable noise estimation. This approach aligns with the definition of the self-referencing method recommended by the ASTM standards for nondestructive testing. A graphical representation is presented in Fig. 4.

Fig. 5 provides an example illustrating the process of noise estimation to account for intensity scale variations between images. In Fig. 5(a), a cropped image from the third principal component of the PCT for a thermographic inspection with four artificial defects is shown. The image is visibly affected by noise. Fig. 5(b) demonstrates the result of applying a standard deviation filter, highlighting edge regions. In contrast, Fig. 5(c) presents the results of applying a median filter to the previous image, offering a smoother estimation of noise that more accurately reflects the noise distribution within the original image while removing the influence of the edges. The noise estimated for each pixel across various spatial scales is utilized to compensate for intensity scale variations between images. This process ensures a more consistent assessment of the contrast, allowing for characterization regardless of the inherent differences in intensity across the various types of images.

3.3. Calculation of the condensed images

The MS−CNR is applied to each image in the combined sequence, and the resulting values are subsequently utilized to extract condensed images, which include the Maxigram, Sigmagram, Sourcegram, and Timegram.

3.3.1. Maxigram

The Maxigram is calculated for a sequence of images I_i, where i represents the image number in the combined sequence. It is determined by selecting the maximum MS-CNR across all images, thereby effectively highlighting the regions of highest contrast across space, scale, and time (represented as frames in the sequence). This approach enhances the visibility of defects and anomalies by consolidating the most relevant information from the entire sequence. The Maxigram, Mg, can be expressed as (10).

$$Mg = \max_i \text{MS−CNR}(I_i) \tag{10}$$

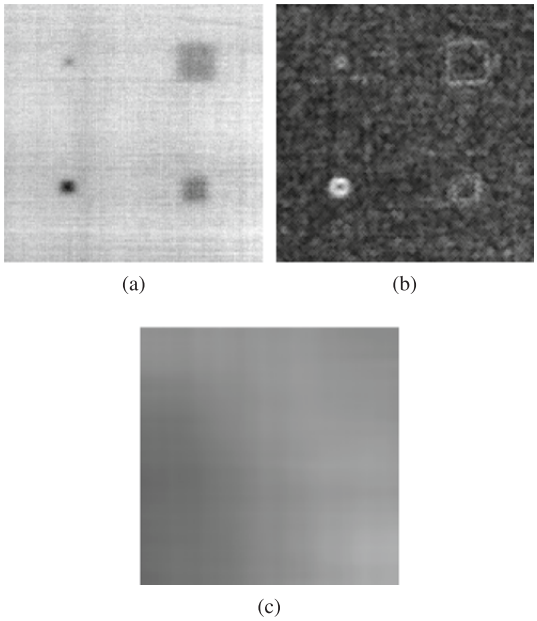

Fig. 5. Estimation of noise to compensate for intensity scales between images. (a) Image. (b) Standard deviation filter. (c) Windowed median, the final estimated background noise for each pixel (σ_N).

3.3.2. Sigmagram

The Sigmagram is defined as the set of sigma values for each pixel at which the maximum MS-CNR is observed. This metric effectively indicates the scale at which the highest contrast is achieved for each pixel, providing valuable information for defect detection and characterization. The Sigmagram, Sig, can be expressed mathematically as (11), where σ_i denotes the sigma value corresponding to the ith image, and Mg is the Maxigram. This formulation captures the sigma values for each pixel where the maximum MS-CNR is found.

$$Sig = \sigma \text{ where } \sigma = \sigma_i \text{ for } i \text{ such that MS-CNR}(I_i) = Mg \tag{11}$$

3.3.3. Sourcegram

The Sourcegram represents the normalized pixel value, ranging between 0 and 1, at the location in the combined sequence where the maximum MS-CNR is observed. Since the different post-processing techniques may produce results with fundamentally different value ranges, for example, one might represent a temporal derivative while another reflects phase information in the frequency domain, a direct combination of raw values could be misleading. Therefore, normalization is necessary to bring these values onto a comparable scale, ensuring that the Sourcegram meaningfully represents the relative intensities across different techniques. This step enables a more coherent interpretation of the fused data. The Sourcegram, Sog, can be expressed mathematically as (12). In this equation, $I_i(x, y)$ is the pixel value from the ith image in the combined sequence, and $\max(I)$ and $\min(I)$ denote the maximum and minimum pixel value across the combined sequence. This formulation captures the normalized pixel values at which the maximum multi-scale contrast-to-noise ratio (MS-CNR) is observed, ensuring that values are scaled between 0 and 1. This formulation accounts for the range of pixel intensities, ensuring proper normalization.

$$Sog = \frac{I_i - \min(I_i)}{\max(I_i) - \min(I_i)}$$
$$\text{where } i \text{ is such that MS-CNR}(I_i) = Mg \tag{12}$$

3.3.4. Timegram

The Timegram represents the frame number within the sequence where the maximum MS-CNR is observed, effectively indicating the specific moment at which the highest contrast-to-noise ratio occurs for each pixel. The Timegram, Tg, can be expressed mathematically as (13)

$$Tg = \arg\max_i \text{MS-CNR}(I_i) \tag{13}$$

3.4. Complementary roles of the condensed images

The four condensed images—Maxigram, Sigmagram, Sourcegram, and Timegram—each extract distinct and complementary information from the sequence, collectively offering a richer and more complete understanding of the detected features:

- Maxigram captures the maximum normalized contrast across multiple spatial scales for each pixel over the entire sequence. This allows it to highlight regions with the highest contrast-to-noise ratio (CNR), making it particularly effective for localizing potential defects. However, it lacks information about the scale at which this contrast occurs, and therefore cannot infer the size of the detected features. This limitation is addressed by the Sigmagram.
- Sigmagram complements the Maxigram by encoding the scale (e.g., spatial resolution or smoothing level) at which the maximum contrast is achieved for each pixel. Since larger defects typically peak at coarser scales and smaller ones at finer scales, the Sigmagram provides valuable insights into the size of the defect. However, it does not reflect the actual intensity or shape of the feature—this information is instead captured by the Sourcegram.
- Sourcegram stores the pixel intensity from the original image frame in which the maximum contrast occurs. As a result, it preserves information about the true shape and texture of the defect, which are not represented in either the Maxigram or Sigmagram. Nevertheless, it does not indicate when in the sequence the maximum contrast occurs, nor does it inform about how the contrast was achieved (i.e., which postprocessing method contributed to it).
- Timegram addresses this gap by recording the time index (or frame number) at which each pixel reaches its maximum contrast. This temporal information captures the evolution of the thermal response over time, providing valuable insights into the material's behavior. In pulsed thermography, for example, the frame of maximum contrast can be correlated with defect depth, while in other applications it may reflect variations in material composition. However, Timegram alone does not convey spatial or intensity information, which is complemented by the Sourcegram and Maxigram representations.

Together, these four representations complement each other:

- The Maxigram localizes high-CNR regions but needs the Sigmagram for size context,
- The Sigmagram adds size information but relies on the Sourcegram for shape and intensity,
- The Sourcegram provides spatial detail but not timing, which the Timegram supplies.

This synergy reduces the reliance on manual inspection and enables more automated and holistic analysis of thermographic sequences.

4. Results and discussion

To evaluate the performance of the proposed approach, it was tested using real data obtained from infrared inspections under different stimulation methods. By analyzing real-world data, the robustness and applicability of the proposed method in detecting and characterizing defects were examined, providing valuable insights into its practical utility in various inspection environments.

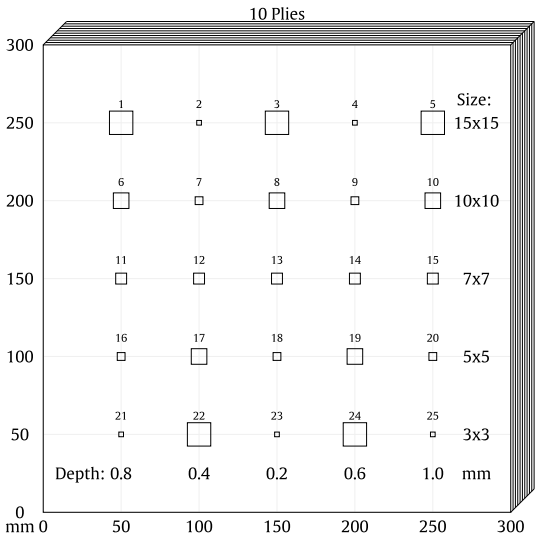

Fig. 6. A model of the inspected specimen using pulsed heating, including detailed information about the positions, sizes, and depths of the defects.

4.1. Test with carbon fiber composite specimen using pulsed heating

To validate the proposed method, infrared inspection images of a carbon fiber reinforced polymer (CFRP) specimen were used. The specimen measured $300 \times 300 \times 2$ mm, consisting of 10 plies. The specimen features 25 square Teflon® inserts, which simulate defects of different sizes (3, 5, 7, 10, and 15 mm) and depths (ranging from 0.2 to 1 mm). The layout of these defects, as depicted in Fig. 6, provides a reference framework for further analysis. Each defect is numbered to facilitate the interpretation of the results.

The inspection of the specimen was conducted using active thermography in reflection mode. Two high-power photographic flashes (Balcar FX 60, 6.4 k), emitting a 2 ms pulse, were employed as heat sources. The thermal data was captured at a rate of 88 Hz using a Phoenix infrared camera from FLIR Systems for 3.5 s. This camera features a resolution of 640×512 pixels, a 14-bit depth per pixel, and an operational wavelength range of 3 to 5 μm. For a more detailed description of the experimental setup, refer to [57].

The raw thermographic sequence recorded during the inspection was processed using various post-processing techniques, including TSR to extract the first and second derivatives, PCT to derive the EOF components, PPT to generate phase images, and PLST to obtain the regression components. Applying each post-processing technique produces a new sequence, making it impractical to display all of them. Fig. 7 highlights some of the most relevant images, presented with a high-contrast color map to ensure that defects of both high and low intensities are visible within a single frame.

Overall, most defects can be effectively identified and appreciated when the results from all the post-processing methods are considered together. Each technique contributes unique insights, compensating for the limitations of others. For instance, while PPT may minimize the effects of non-uniform heating, other methods like PCT or PLST provide better contrast. This integrated analysis emphasizes the importance of leveraging diverse post-processing techniques to achieve a robust and comprehensive defect detection process.

The images generated from the post-processing techniques reveal the impact of non-uniform heating during excitation and the subsequent propagation of heat through the material. These effects result in regions of varying intensity across the images, which can obscure the visibility of defects. The uneven distribution of heat introduces noise and artifacts that complicate the interpretation of thermographic data, particularly for subtle defects. Consequently, this variability poses challenges for accurately identifying and characterizing defects, underscoring the need for robust data fusion and visualization techniques that enhance defect detectability while minimizing the influence of thermal inconsistencies.

No single image from these results offers the best visualization across all defects. While in this case the PPT results appear to be the least influenced by non-uniform heating and likely provide the most consistent visualization, certain defects exhibit better contrast at different frequencies. For example, defect 21 is barely visible in Fig. 7(m), whereas defect 23 is entirely absent. Conversely, Fig. 7(n) highlights defect 23 clearly, but defect 21 is not discernible. For instance, defect 23 is distinctly highlighted in the first and second derivative obtained from TSR processing, exhibiting exceptionally high contrast that surpasses its visibility in the PPT results. This example illustrates how certain post-processing techniques, despite their susceptibility to artifacts like non-uniform heating, can provide superior contrast for specific defects, making them invaluable for a comprehensive analysis. This variation also underscores the complementary nature of the post-processing techniques, as different methods may excel for different defects.

The raw infrared sequence, along with the complete sequences derived from the first and second derivatives, all EOF components from PCT, and the frequency components of the PPT and PLST methods, are combined into a single comprehensive sequence. This unified dataset is then processed using the proposed multi-sequence analysis method. In this example, the range of sigma values was determined based on the minimum and maximum anticipated defect sizes, ensuring effective detection across the spectrum of possible features considering image resolution. Specifically, Convolution kernel sizes were specifically chosen to range from 5 to 50 pixels. This range ensures that the smallest kernel size is slightly smaller than the minimum defect size, allowing for the detection of finer details, while the largest kernel size exceeds the maximum defect size, capturing broader features effectively. This selection strikes a balance between covering the full spectrum of defect sizes and maintaining computational efficiency. The corresponding sigma values for the Gaussian function were calculated using the relationship (14) where the kernel size defines the extent of the Gaussian smoothing window, and σ represents the standard deviation. This formula ensures that the kernel encompasses approximately 99% of the Gaussian distribution, effectively balancing spatial resolution and smoothing. By tailoring the kernel sizes and their associated sigma values to the defect characteristics, the method adapts dynamically to the needs of the inspection process, providing robust contrast evaluation across a range of defect scales.

$$\sigma = \frac{\text{kernel size} - 1}{2\sqrt{2\ln(2)}} \tag{14}$$

The processing of the multi-sequence using the proposed methods takes approximately 2 min on a modern computer with the selected configuration, which represents a negligible cost compared to the time and expertise required for manual inspection of dozens or even hundreds of images generated by conventional post-processing techniques. Importantly, the selected range of sigma values was carefully optimized to balance computational efficiency and defect detectability. Extending this range would increase processing time without providing additional benefits, as the chosen configuration already ensures coverage of the relevant defect sizes while maintaining manageable computation. In this sense, the proposed condensed representations (Maxigram, Sigmagram, Sourcegram, and Timegram) do not merely add computational complexity, but rather substitute extensive manual exploration of multiple phasegrams and components with a small, automated overhead. While phasegrams themselves can offer clear defect visualization in some cases, they require operators to examine many frequency components to identify the most relevant one for each defect. By contrast, our approach consolidates complementary information from PPT and other techniques into a few images that highlight all defects simultaneously,

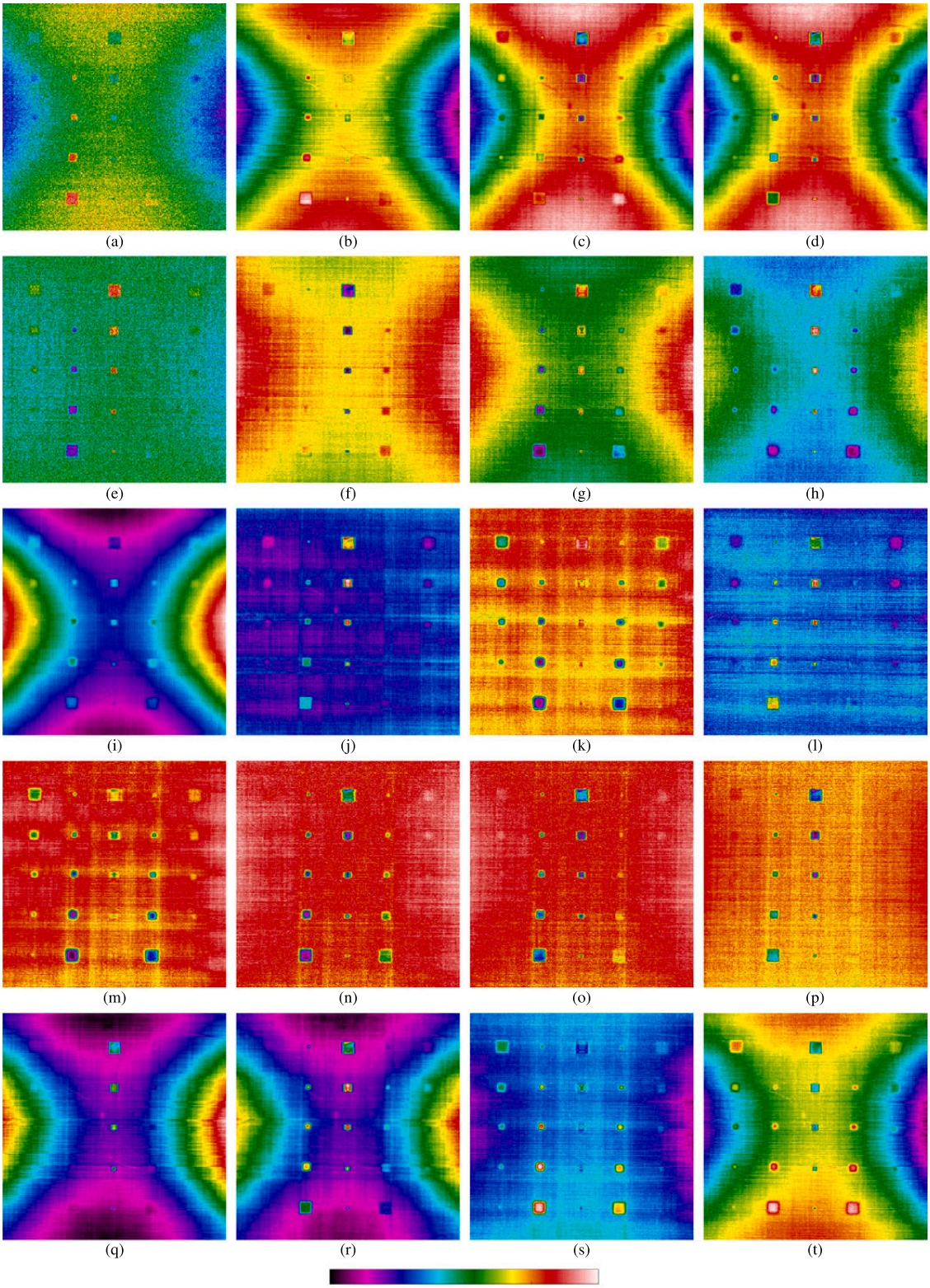

Fig. 7. Results of the inspection for the carbon fiber composite specimen using pulsed heating. (a), (b), (c), (d) First derivative at time 0.1, 0.45, 0.9, 1.12, 1.6 s. (e), (f), (g), (h) Second derivative at time 0.1, 0.45, 0.9, 1.12, 1.6 s. (i), (j), (k), (l) EOF 1, 2, EOF 3 and 4. (m), (n), (o), (p) four lowest frequencies of the PPT. (q), (r), (s), (t) PLST at time 0.1, 0.45, 0.9, 1.12, 1.6 s.

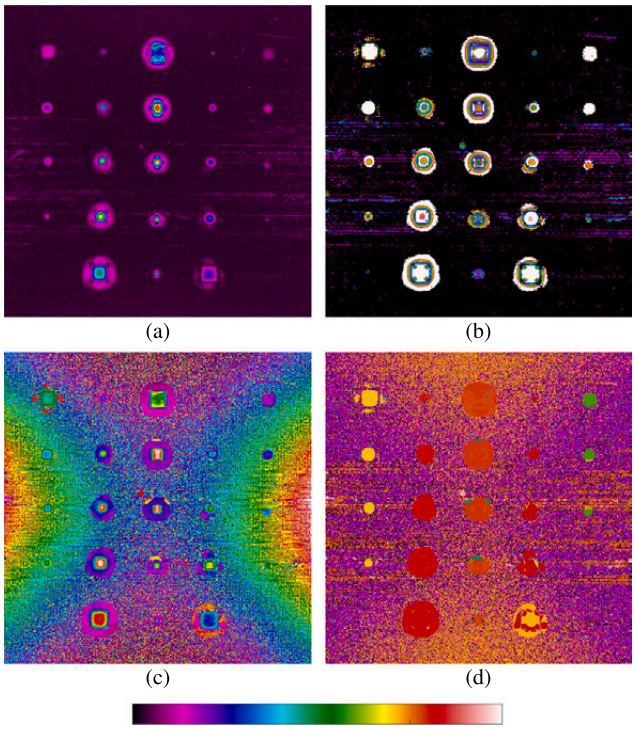

Fig. 8. Results of the proposed method for the carbon fiber composite specimen using pulsed heating. (a) Maxigram. (b) Sigmagram. (c) Sourcegram. (d) Timegram.

thereby reducing human workload, minimizing the risk of oversight, and ensuring robustness in scenarios where methods such as PPT alone is insufficient. Consequently, the additional computations are fully justified, as they streamline the analysis process, enhance interpretability, and provide more reliable and complete inspection results.

The resulting outputs—Maxigram, Sigmagram, Sourcegram, and Timegram—are presented in Fig. 8, showcasing the enhanced capability of the proposed approach to integrate information from multiple post-processing techniques.

The results presented in Fig. 8 demonstrate that both the Maxigram and Sigmagram effectively highlight the defects in a single image, mitigating the impact of non-uniform heating and providing exceptionally high contrast. In both images, the background remains highly uniform with minimal noise, significantly enhancing defect visibility.

The Sourcegram preserves the actual geometry of the defects, which makes it particularly suitable for estimating their size. A rigorous quantitative evaluation would require camera calibration [58], followed by image segmentation and conversion of pixel coordinates into world units, allowing direct comparison with the known defect dimensions. Such measurements would necessarily depend on the segmentation method, image resolution, and calibration accuracy. Although this procedure was not carried out in the present study, a qualitative validation was performed by overlapping the Sourcegram with the results of derivative-based post-processing techniques that delineate defects with sharp and well-defined edges. This comparison confirmed that the defect sizes observed in the Sourcegram are consistent with those revealed by these methods, supporting its reliability for size estimation. Moreover, when combined with the Maxigram and Sigmagram, the Sourcegram, although more susceptible to noise, provides valuable complementary information: the former enhance defect visibility through contrast, while the latter preserves the true geometry, together enabling both robust detection and accurate determination of defect dimensions.

In comparison to analyzing the results of multiple post-processing techniques, the Maxigram and Sigmagram offer a considerable advantage by consolidating crucial information into a single image. This significantly streamlines the analysis process, as there is no need to evaluate each post-processing result separately, especially considering that each result consists of numerous images, any of which could be of interest. By presenting the most relevant data in one image, these methods reduce the complexity and time needed for inspection, ensuring quicker and more efficient defect detection.

The Maxigram and Sigmagram not only simplify the workflow but also offer a clear and consistent visualization of defects. They reduce the complexity and time required for inspection while maintaining high-quality images with low noise, high contrast, and eliminating variations caused by non-uniform heating. This makes them highly effective tools for inspection analysis, as they remove the need for manual comparison across various processing methods, ensuring faster, more reliable, and consistent defect detection.

The Timegram, shown in Fig. 8(d), illustrates the frame number at which the maximum contrast is achieved, offering additional insights that complement the previous images. Beyond this, it also provides valuable information about which post-processing technique yields the best contrast for each defect. By adjusting the colors in this figure for each individual sequence in the combined dataset, the results can be presented graphically, clearly highlighting the most effective method for visualizing the defects, as can be seen in Fig. 9. This figure visually represents the selected post-processing technique and the corresponding frame where the maximum contrast is achieved for each pixel, using a color-coded scheme for interpretability.

Fig. 9 represents with different color the post-processing technique that provides the best contrast for each pixel. As can be seen, in this case the PLST provides the best contrast for most defects, while the second derivative and PCT offer the best contrast for most of the remaining defects. Surprisingly, the phase images obtained using the PPT only yield the best contrast for defect number 24. This suggests that, although a qualitative comparison of the resulting images from each post-processing technique may indicate that phase images might perform best (as they are less affected by non-uniform heating), the highest contrast for different defects is achieved using a combination of different post-processing techniques, not including the PPT in this case.

In sound areas, different types and magnitudes of noise are present, which affect each post-processing technique differently. Consequently, the technique that produces the highest apparent contrast at a given location may simply reflect random noise rather than meaningful information. For this reason, Fig. 9 should be interpreted in conjunction with the Maxigram. In regions where the Maxigram shows very low contrast, the variations observed for the best post-processing technique are likely due to noise and can be disregarded.

To quantitatively compare the results, signal-to-noise ratio (SNR) values are calculated from the multi-sequence generated by combining all considered post-processing techniques, and also from the Maxigram and Sigmagram. In the multi-sequence, the best SNR for each defect is calculated as the maximum value for that defect across all frames in the sequence. This approach ensures that the highest possible contrast is captured, reflecting the optimal visibility of the defect throughout the sequence. The SNR is determined using the formula in (15), where μ_S is the average signal level in the defect region, μ_N is the average noise level in the reference or sound region, σ_S is the standard deviation of the signal in the defect region, and σ_N is the standard deviation of the noise in the reference region. The results are represented in Fig. 10.

$$SNR = \frac{|\mu_S - \mu_N|}{\sigma_N} \tag{15}$$

The SNR results shown in Fig. 10 indicate that the Maxigram and Sigmagram outperform other techniques in 18 of the 25 defects, providing the highest SNR values. The only notable exception is defect

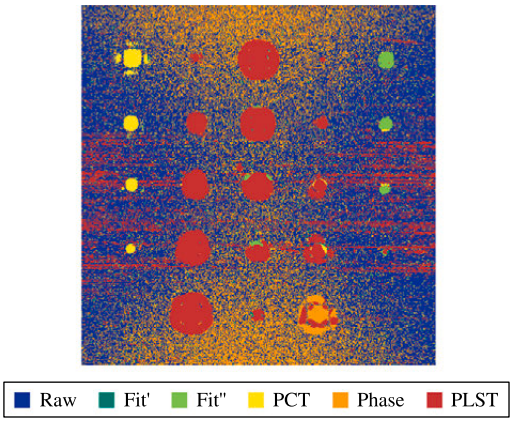

Fig. 9. Post-processing technique that provides the best contrast for the carbon fiber composite specimen using pulsed heating.

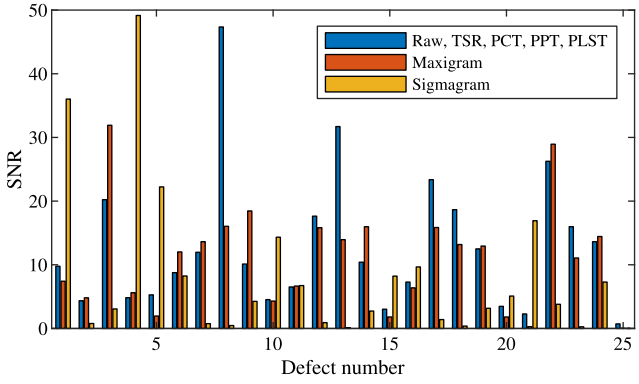

Fig. 10. SNR for the combined sequence of post-processing methods, Maxigram and Sigmagram.

number 25, which remains undetected with almost also negligible SNR in the combined sequence. Defect number 25, being only 3 × 3 mm with a depth of 1 mm, presents a significant challenge for detection due to its small size and shallow depth. As shown in the results, this defect remains undetected across all post-processing methods, with the resulting SNR values being negligible, demonstrating that the defect is effectively indistinguishable from the surrounding noise. This limitation lies more in the inherent characteristics of infrared thermography and the sensitivity of resolution of the camera used, which struggles to generate sufficient thermal contrast for such small and shallow defects, rather than in the post-processing techniques themselves. The proposed multi-sequence fusion approach relies on infrared thermography's ability to produce detectable thermal contrast, which is compromised in the case of defect 25. For all other defects, the SNR values are either higher or comparable, making detection possible. Moreover, the SNR results from the Maxigram and Sigmagram are obtained from single images rather than a sequence, allowing them to be viewed simultaneously in a single image. This highlights their efficiency in detecting defects easily, ensuring quick and accurate analysis.

4.2. Test with carbon fiber composite specimen using step heating

A second composite specimen made of carbon fiber was also used to assess the results. This specimen features deeper defects, making them more challenging to detect. It consists of several layers of carbon fiber, each with fibers oriented in a specific direction, which are stacked and bonded together with resin. Internal defects were introduced using small sheets of polytetrafluoroethylene (PTFE) and metal shavings.

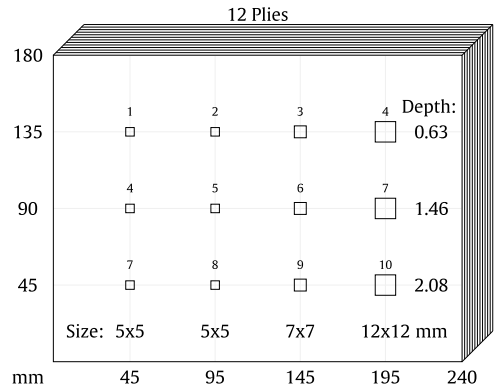

Fig. 11. A model of the inspected specimen using step heating, including detailed information about the positions, sizes, and depths of the defects.

The PTFE simulates delaminations, which occur when adjacent plies separate, while the metal shavings represent accidental inclusions of small cutting tool fragments during the manufacturing process. The 12 subsurface defects are distributed as shown in Fig. 11. These defects vary in size and depth, with the 12 × 12 mm defect at a depth of 0.63 mm being the easiest to detect, and the 5 × 5 mm defect at a depth of 2.08 mm being the most difficult.

The inspection was conducted in reflection mode using a Xenix Gobi 640 GigE infrared camera over a 20-s period, with the specimen being heated for 10 s. This camera features a resolution of 640 × 480 pixels, a 16-bit depth per pixel, and an operational wavelength range of 8 to 14 μm. The camera was positioned 1.5 m away from the specimen, while two halogen lamps were placed 1.6 m from it. The video was recorded at 50 frames per second, resulting in a total of 1000 frames captured. Additional details about the experimental setup can be found in [28].

Following a similar approach as with the previous specimen, the raw sequence was processed using a range of post-processing techniques, including TSR for extracting the first and second derivatives, PCT for deriving the EOF components, PPT for generating phase images, and PLST for regression components. Fig. 12 presents some of the most relevant images from this analysis.

The results from this specimen underscore the increased challenges in defect detectability due to its greater depth and more complex conditions. Unlike the previous specimen, where defects were more easily observable, the deeper and more intricate defects in this case are much harder to detect. Most images allow for the detection of only the shallower defects, while the deeper ones remain difficult to identify, even with the high-contrast color maps applied. Recognizing these deeper defects often requires expertise and careful inspection, as their subtlety makes them more challenging to distinguish, highlighting the limitations of the imaging methods in such complex scenarios.

Once again, the images are impacted by non-uniform heating and noise, which further complicates defect detection. For instance, in the PLST results, deeper defects are barely visible, and their detection becomes extremely difficult due to the high-intensity region caused by excessive heating in this area. Similarly, the PPT results in this case are also influenced by these irregularities, making detection more challenging. In contrast, the PCT technique proves to be more resilient to these issues in this case, showing the least impact from non-uniform heating. In this case, the second derivative appears to provide the best contrast for certain defects. Its ability to highlight subtle changes in intensity allows for better visualization of these defects, even in areas where other post-processing techniques struggle due to non-uniform heating or noise.

The raw infrared sequence, along with the complete sequences generated from the various post-processing techniques, are combined

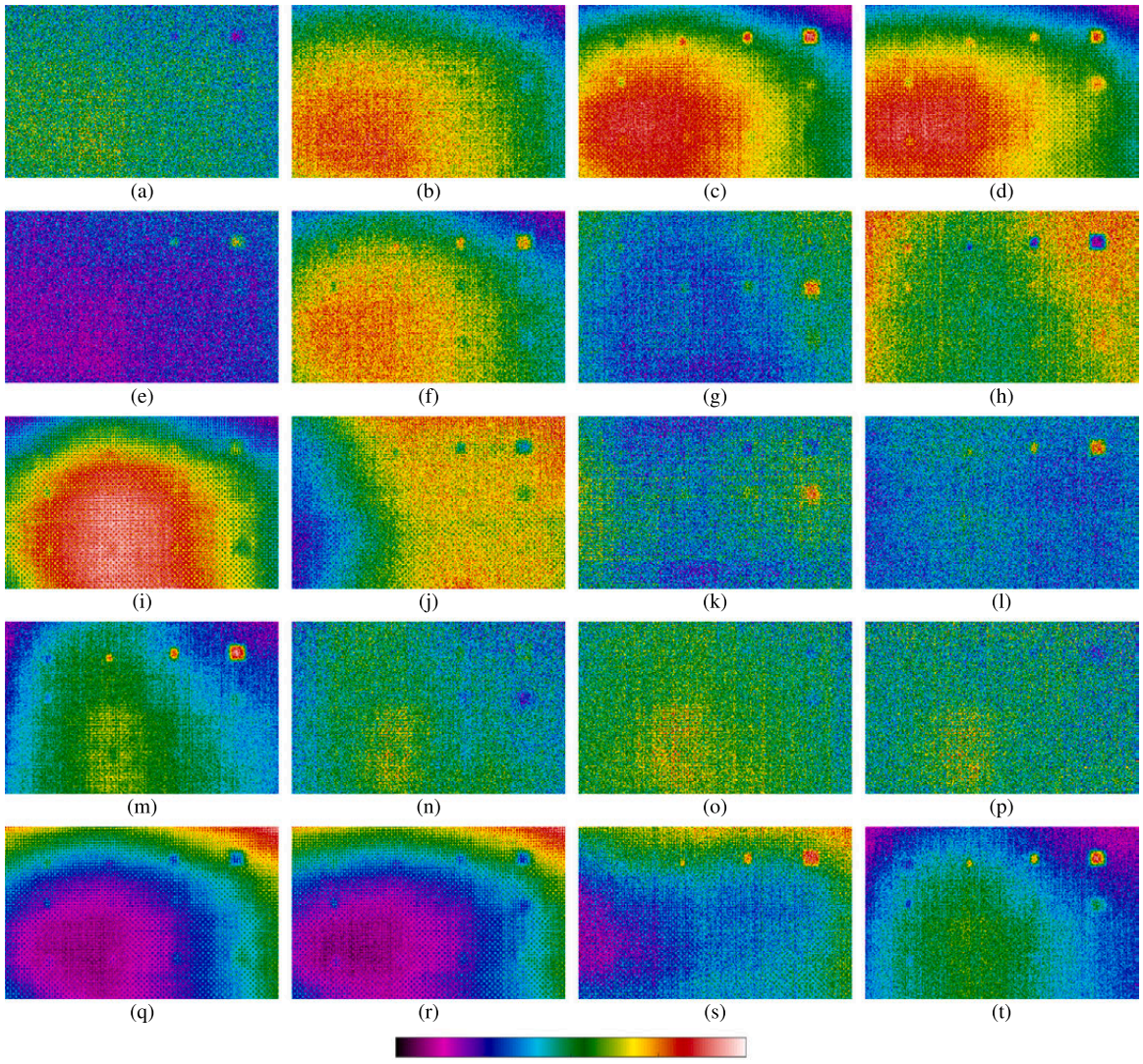

Fig. 12. Results of the inspection for the carbon fiber composite specimen using step heating. (a), (b), (c), (d) First derivative at time 0.1, 0.45, 0.9, 1.12, 1.6 s. (e), (f), (g), (h) Second derivative at time 0.1, 0.45, 0.9, 1.12, 1.6 s. (i), (j), (k), (l) EOF 1, 2, EOF 3 and 4. (m), (n), (o), (p) four lowest frequencies of the PPT. (q), (r), (s), (t) PLST at time 0.1, 0.45, 0.9, 1.12, 1.6 s.

into a single comprehensive sequence and processed using the proposed method and a similar configuration for the range of sigma values. The resulting images can be seen in Fig. 13.

The results presented in Fig. 13 highlight the advantages of the proposed approach. It not only integrates the best results from all the post-processing techniques but also generates single, easily analyzable images that emphasize the highest contrast while maintaining a uniform background. In this case, the combination of the Maxigram and Sigmagram proves highly effective for accurately and easily identifying the positions of all the defects in the specimen—an achievement that would not be possible using the individual post-processing techniques alone. Using the proposed approach, and even with some artifacts caused by noise, any technician could easily identify all the defects. The clear contrast and uniform background provided by the Maxigram and Sigmagram enable straightforward defect detection, minimizing the challenges typically posed by noise and non-uniform heating.

The Sourcegram and Timegram, in this case, result in images with increased noise. However, the additional information they provide, when combined with the Maxigram and Sigmagram, enhances the understanding of the size and position of the defects.

The results in Fig. 14, which represent the post-processing techniques that provide the best contrast, show that for most of the defects in this specimen, the second derivative yields the best results. This finding contrasts with our previous observations, where PLST and PCT were identified as the most effective techniques. This highlights the necessity of combining multiple post-processing techniques in order to achieve the most reliable and comprehensive results.

Fig. 15 presents a quantitative comparison of SNR for this specimen. The proposed approach achieves better SNR in 11 out of the 12 defects. The only exception is defect number 1, where the SNR is slightly higher in the sequence, although the difference is negligible. The results once again demonstrate the effectiveness of the proposed approach, not only by streamlining defect detectability and presenting all defects with good contrast in a single image, but also by providing superior SNR values.

Fig. 15 presents a quantitative comparison of the SNR for defects of varying sizes and depths. The heatmaps illustrate the SNR distribution for post-processing methods compared with the proposed approach, highlighting differences in detectability across the range of defect parameters. Each cell represents the measured SNR for a specific combination of defect size and depth, with higher values indicating improved defect detectability. The shared color scale allows a direct comparison between the two methods. The SNR distribution for post-processing methods shows relatively low values across all defect sizes

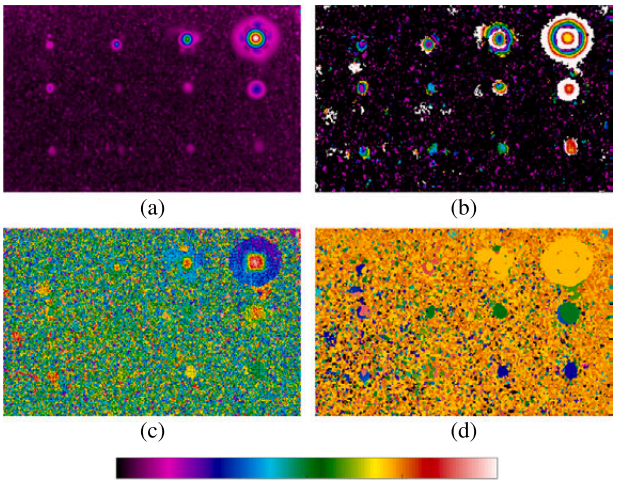

Fig. 13. Results of the proposed method for the carbon fiber composite specimen using step heating. (a) Maxigram. (b) Sigmagram. (c) Sourcegram. (d) Timegram.

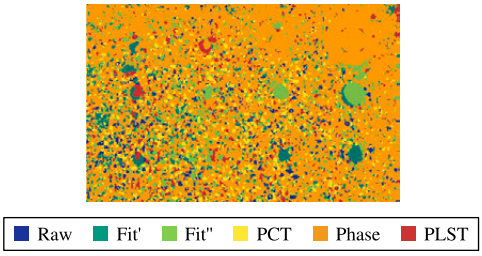

Fig. 14. Post-processing technique that provides the best contrast for the carbon fiber composite specimen using step heating.

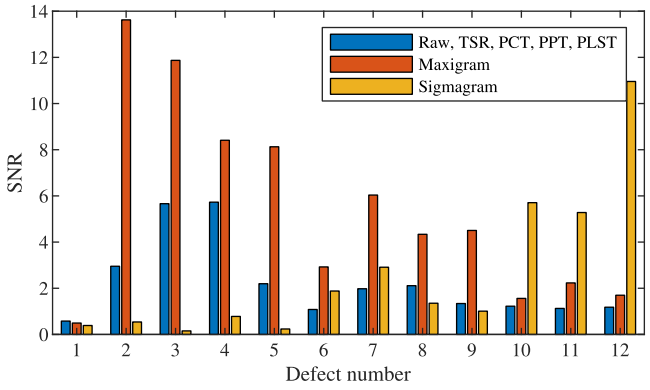

Fig. 15. SNR comparison for the carbon fiber composite specimen using step heating.

and depths, ranging approximately from 0.5 to 5.7, indicating limited defect detectability. In contrast, the proposed method achieves significantly higher SNR values for most defect combinations, reaching up to 13.6, which demonstrates improved detectability, particularly for medium to large defects. This difference highlights the enhanced sensitivity of the proposed method.

The enhanced SNR values achieved by the proposed method correlate with better defect detectability This implies that the proposed method enables more reliable detection of smaller or deeper defects, thereby improving the overall effectiveness of non-destructive evaluation processes. Furthermore, the proposed method provides the SNR results in single images (Maxigram and Sigmagram), rather than in a

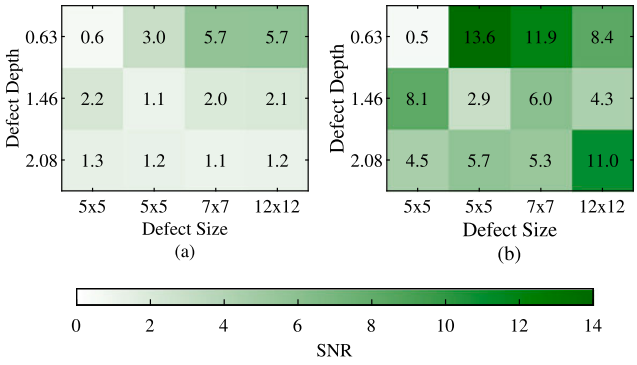

Fig. 16. Comparison of SNR for defects across different sizes and depths. (a): Raw, TSR, PCT, PPT, PLST. (b): Maxigram and Sigmagram.

sequence, allowing for simultaneous viewing of all defects in one image. This highlights the efficiency of the proposed method in facilitating quick and accurate analysis (see Fig. 16).

While the primary focus of this study is on improving defect detectability through the fusion of multiple post-processing methods, the analysis of the SNR results provides indirect evidence regarding the potential improvement in depth-to-diameter ratio detection capability. As shown in Fig. 15, the proposed method consistently achieves higher SNR values compared to the conventional approach across most defect combinations, with peaks reaching 13.6, whereas the baseline remains below 6. This increased contrast indicates that the proposed fusion method enhances the visibility of subtle defects. The observed SNR enhancement provides strong evidence that the proposed approach can improve the precision of defect characterization and support more reliable defect detection in practical applications.

In the experiments two different excitation methods are used: pulsed and step heating. Both heating methods reveal complementary strengths: pulsed heating offers a rapid excitation well-suited for shallow defect detection, while step heating provides a more sustained thermal input, enhancing detectability at greater depths. It is also important to consider the differences in energy supplied during pulsed and step heating thermography. In pulsed thermography, a high-energy pulse is applied over a very short duration, resulting in a rapid surface temperature increase and strong thermal contrast for shallow defects. In contrast, step heating delivers a lower power input over an extended period, producing a more gradual temperature rise that allows deeper defects to develop observable thermal gradients, but may reduce contrast for shallower defects. These differences in energy delivery affect the detectability of defects depending on their depth and the thermal properties of the material. The multi-sequence fusion approach demonstrated robustness under both conditions, but the optimal post-processing technique selected varied depending on the heating method and defect characteristics. This highlights the adaptability of the proposed framework to different excitation scenarios and its potential to unify insights from varied thermal loading strategies.

4.3. Comparison with wavelet-based image fusion

Fig. 17 presents the results of an alternative wavelet-based image fusion method proposed in [25]. A qualitative comparison between these results and those obtained using the proposed approach, particularly when examining the Maxigram and Sigmagram representations, clearly demonstrates the superior defect detectability of the proposed method. For the first specimen, the wavelet-based fusion reveals only the most prominent defects, while for the second specimen, almost no defects are discernible. In contrast, as shown in Figs. 13 and 8, the proposed method allows defects to be easily identified across both specimens.

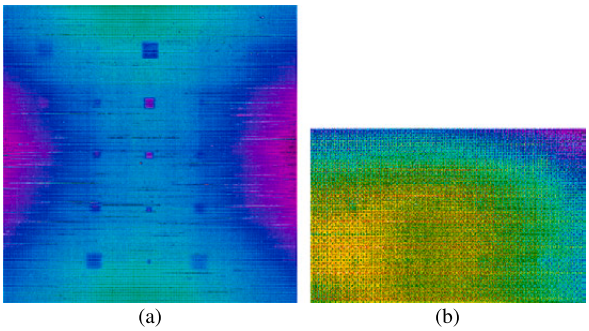

Fig. 17. Results of the wavelet-base image fusion. (a) Image from the carbon fiber composite specimen using pulsed heating. (b) carbon fiber composite specimen using step heating.

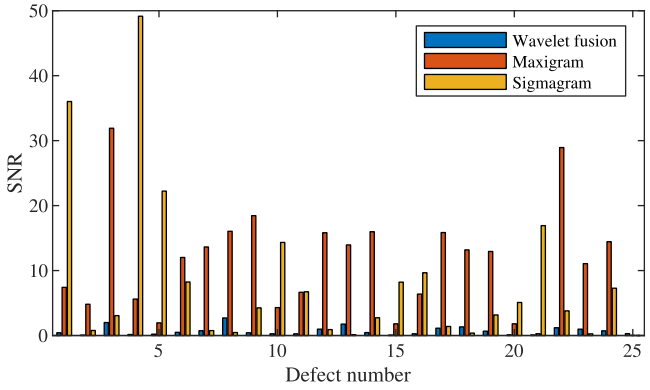

Fig. 18. SNR comparison for the wavelet-based image fusion applied to the carbon fiber composite specimen using pulsed heating.

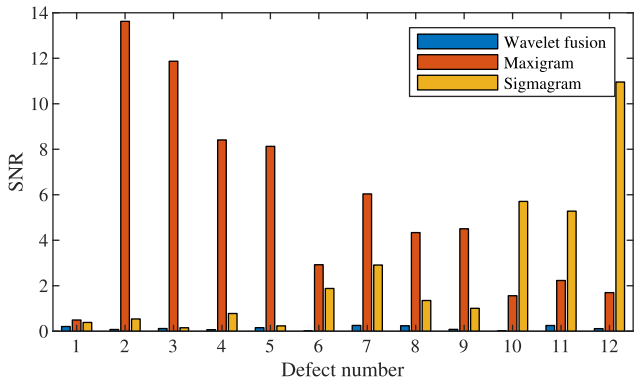

Fig. 19. SNR comparison for the wavelet-based image fusion applied to the carbon fiber composite specimen using step heating.

Figs. 18 and 19 provide a quantitative comparison of the signal-to-noise ratio (SNR) for both specimens, using the wavelet-based image fusion and the proposed approach. As shown, the proposed method clearly outperforms the wavelet-based fusion, achieving substantially higher SNR values across all cases.

Overall, both the qualitative and quantitative results demonstrate that the proposed approach significantly outperforms the wavelet-based fusion, providing markedly enhanced defect visibility and clarity. The improvement is evident across all examined specimens and defect types, indicating that the proposed method not only highlights even subtle defects more effectively but also produces more consistent and reliable results. This indicates that the proposed approach offers significant advantages for practical applications in non-destructive evaluation, outperforming previous methods in scenarios where accurate defect detection and clear visualization are essential for reliable quality assessment and informed decision-making.

5. Conclusion

This study presents an innovative approach for combining multiple sequences obtained from different post-processing techniques into single images that significantly enhance defect detection in active infrared thermography. By leveraging advanced post-processing methods such as TSR, PCT, PPT, and PLST, the proposed multi-sequence framework not only improves the visibility of defects but also optimizes the signal-to-noise ratio (SNR), providing clearer, more accurate results. The Maxigram and Sigmagram, generated from this approach, offer excellent contrast and uniform backgrounds, making them highly effective for defect identification across a variety of specimen types, including those with deep or complex defects. The proposed approach is designed to be generic and not specific to any particular type of defect or excitation method.

The key advantage of this method lies in its ability to simplify the interpretation process by consolidating multiple frames from different post-processing techniques into cohesive, easily interpretable images. The SNR analysis demonstrated that the proposed approach consistently outperforms traditional methods, with improved defect visibility and minimal interference from non-uniform heating and noise. The Maxigram and Sigmagram, in particular, provide better defect contrast in a single image, offering a significant time-saving advantage over sequence-based methods that require multiple frames to be analyzed.

The proposed multi-sequence approach demonstrates a highly effective and efficient solution for defect detection, offering improved SNR, higher defect visibility, and a streamlined analysis process. Because the method is based on contrast behavior across multiple scales and frames, it has been effectively applied to a wide variety of defect types without requiring prior knowledge or customization. This generality makes the approach robust and adaptable for diverse non-destructive testing scenarios. This innovative method holds significant potential for widespread adoption in industrial applications, including quality control, inspection, and monitoring of composite structures and various other materials. Additionally, its principles could be extended to other non-destructive testing techniques, further broadening its scope and impact.

While the proposed method improves defect detectability by leveraging multi-sequence fusion and spatially adaptive analysis, it has certain limitations. Its effectiveness depends on the quality of the results obtained from the underlying post-processing techniques, and the use of multiple sequences and multi-scale analysis introduces computational overhead that may challenge real-time or resource-constrained applications. Moreover, the method has so far been validated only on a limited set of samples with controlled geometries and defect types, which restricts its generalizability. Future research will focus on extending validation to larger and more heterogeneous datasets, integrating advanced post-processing and machine learning techniques, and developing strategies to optimize computational performance for efficient, real-time industrial deployment.

CRediT authorship contribution statement

R. Usamentiaga: Writing – review & editing, Writing – original draft, Visualization, Validation, Supervision, Software, Resources, Project administration, Methodology, Investigation, Funding acquisition, Formal analysis, Data curation, Conceptualization. **S. Sfarra:** Writing – review & editing. **C. Ibarra-Castanedo:** Writing – review & editing. **H. Zhang:** Writing – review & editing. **X. Maldague:** Writing – review & editing.

Declaration of competing interest

The authors declare the following financial interests/personal relationships which may be considered as potential competing interests: Ruben Usamentiaga reports financial support was provided by Spanish National Program for Mobility of Professors and Researchers. Ruben Usamentiaga reports financial support was provided by Spanish National Research Council. If there are other authors, they declare that they have no known competing financial interests or personal relationships that could have appeared to influence the work reported in this paper.

Acknowledgments

This research was partially funded by the Spanish National Program for Mobility of Professors and Researchers, reference PRX22/00165, and projects PID2021-124383OB-I00 and SEK-25-GRU-GIC-24-003.

Data availability

Data will be made available on request.

References

[1] Usamentiaga R, Venegas P, Guerediaga J, Vega L, Molleda J, Bulnes FG. Infrared thermography for temperature measurement and non-destructive testing. Sensors 2014;14(7):12305–48.
[2] Osornio-Rios RA, Antonino-Daviu JA, de Jesus Romero-Troncoso R. Recent industrial applications of infrared thermography: A review. IEEE Trans Ind Informatics 2018;15(2):615–25.
[3] Balakrishnan GK, Yaw CT, Koh SP, Abedin T, Raj AA, Tiong SK, Chen CP. A review of infrared thermography for condition-based monitoring in electrical energy: Applications and recommendations. Energies 2022;15(16):6000.
[4] Wang J, Ou J, Fan Y, Cai L, Zhou M. Online monitoring of electrical equipment condition based on infrared image temperature data visualization. IEEJ Trans Electr Electron Eng 2022;17(4):583–91.
[5] Kim H, Lamichhane N, Kim C, Shrestha R. Innovations in building diagnostics and condition monitoring: A comprehensive review of infrared thermography applications. Buildings 2023;13(11):2829.
[6] Ring E, Ammer K. The technique of infrared imaging in medicine, in infrared imaging: a casebook in clinical medicine. UK: IoP Publishing Bristol; 2015, 1–1.
[7] Ciprián-Sánchez JF, Ochoa-Ruiz G, Gonzalez-Mendoza M, Rossi L. Fire-gan: a novel deep learning-based infrared-visible fusion method for wildfire imagery. Neural Comput Appl 2023;1–13.
[8] Usamentiaga R, García DF. Infrared thermography sensor for temperature and speed measurement of moving material. Sensors 2017;17(5):1157.
[9] Li Z, Pei Y, Qu C, Yang F. A position and attitude measurement method based on laser displacement sensor and infrared vision camera. IEEE Trans Instrum Meas 2022;71:1–9.
[10] Wilcox LM, Donnell KM. Modified thermographic signal-to-noise ratio for active microwave thermography. IEEE Trans Instrum Meas 2024.
[11] Qu Z, Jiang P, Zhang W. Development and application of infrared thermography non-destructive testing techniques. Sensors 2020;20(14):3851.
[12] Pereira Barella B, Garcia Rosa R, Maira Barbosa de Oliveira G, Fernandes H. Enhancing fault characterisation in composites using infrared thermography: a bee colony optimisation approach with self-organising maps. Quant InfraRed Thermogr J 2024;1–19.
[13] Meola C, Boccardi S, Carlomagno GM. Infrared thermography in the evaluation of aerospace composite materials: infrared thermography to composites. Woodhead Publishing; 2016.
[14] Zhu J, Mao Z, Wu D, Zhou J, Jiao D, Shi W, Zhu W, Liu Z. Progress and trends in non-destructive testing for thermal barrier coatings based on infrared thermography: A review. J Nondestruct Eval 2022;41(3):49.
[15] Maldague XP. Nondestructive evaluation of materials by infrared thermography. Springer Science & Business Media; 2012.
[16] Pozzer S, El Refai A, López F, Ibarra-Castanedo C, Maldague X. Passive infrared thermography for subsurface delamination detection in concrete infrastructure: Inference on minimum requirements. Comput Struct 2024;305:107529.
[17] Usamentiaga R, Fernandez MA, Villan AF, Carus JL. Temperature monitoring for electrical substations using infrared thermography: architecture for industrial internet of things. IEEE Trans Ind Informatics 2018;14(12):5667–77.
[18] Madruga FJ, Ibarra-Castanedo C, Conde OM, López-Higuera JM, Maldague X. Infrared thermography processing based on higher-order statistics. NDT & E Int 2010;43(8):661–6.
[19] Ibarra-Castanedo C, Maldague X. Pulsed phase thermography reviewed. Quant Infrared Thermogr J 2004;1(1):47–70.
[20] Rajic N. Principal component thermography for flaw contrast enhancement and flaw depth characterisation in composite structures. Compos Struct 2002;58(4):521–8.
[21] Shepard SM, Lhota JR, Rubadeux BA, Wang D, Ahmed T. Reconstruction and enhancement of active thermographic image sequences. Opt Eng, Bellingham 2003;42(5):1337–42.
[22] Usamentiaga R, Venegas P, Guerediaga J, Vega L, López I. A quantitative comparison of stimulation and post-processing thermographic inspection methods applied to aeronautical carbon fibre reinforced polymer. Quant InfraRed Thermogr J 2013;10(1):55–73.
[23] Lema DG, Pedrayes OD, Usamentiaga R, García DF. Improved detection of subsurface defects through active thermography and ensembling techniques. Qual Eng 2023;35(4):669–85.
[24] Ibarra-Castanedo C, Sfarra S, Klein M, Maldague X. Solar loading thermography: Time-lapsed thermographic survey and advanced thermographic signal processing for the inspection of civil engineering and cultural heritage structures. Infrared Phys Technol 2017;82:56–74.
[25] Ghali V, Suresh B, Hemanth A. Data fusion for enhanced defect detectability in non-stationary thermal wave imaging. IEEE Sensors J 2015;15(12):6761–2.
[26] Gholizadeh S. Deep learning and machine learning techniques in advanced non-destructive testing. J Harbin Eng Univ 2023;44(11):977–93.
[27] Khanafer M, Shirmohammadi S. Applied ai in instrumentation and measurement: The deep learning revolution. IEEE Instrum Meas Mag 2020;23(6):10–7.
[28] Lema DG, Pedrayes OD, Usamentiaga R, Venegas P, García DF. Automated detection of subsurface defects using active thermography and deep learning object detectors. IEEE Trans Instrum Meas 2022;71:1–13.
[29] Wei C, Han H, Wu Z, Xia Y, Ji Z. Transformer-based multi-scale reconstruction network for defect detection of infrared images. IEEE Trans Instrum Meas 2024.
[30] Wu H, Huang X, He C, Xiao H, Luo S. Infrared small target detection with swin transformer-based multi-scale atrous spatial pyramid pooling network. IEEE Trans Instrum Meas 2024.
[31] Pedrayes OD, Lema DG, Usamentiaga R, Venegas P, García DF. Semantic segmentation for non-destructive testing with step-heating thermography for composite laminates. Measurement 2022;200:111653.
[32] Lema DG, Usamentiaga R, García DF. Enhancing automated inspection in metal industries: zero-shot segmentation of surface defects using bounding box prompts. Meas Sci Technol 2024;35(8):085604.
[33] Zou Y, Zhang L, Liu C, Wang B, Hu Y, Chen Q. Super-resolution reconstruction of infrared images based on a convolutional neural network with skip connections. Opt Lasers Eng 2021;146:106717.
[34] Huang Y, Jiang Z, Lan R, Zhang S, Pi K. Infrared image super-resolution via transfer learning and psrgan. IEEE Signal Process Lett 2021;28:982–6.
[35] Marani R, Palumbo D, Galietti U, Stella E, D'Orazio T. Enhancing defects characterization in pulsed thermography by noise reduction. NDT & E Int 2019;102:226–33.
[36] Doshvarpassand S, Wu C, Wang X. An overview of corrosion defect characterization using active infrared thermography. Infrared Phys Technol 2019;96:366–89.
[37] Garrido I, Lagüela S, Otero R, Arias P. Thermographic methodologies used in infrastructure inspection: A review—post-processing procedures. Appl Energy 2020;266:114857.
[38] Wu D, Wang Y, Miao Z, Wu C. An improved infrared image post-processing method for metals and composites. Infrared Phys Technol 2024;142:105576.
[39] Poelman G, Hedayatrasa S, Segers J, Van Paepegem W, Kersemans M. Multi-scale gapped smoothing algorithm for robust baseline-free damage detection in optical infrared thermography. NDT & E Int 2020;112:102247.
[40] Panella F, Pirinu A, Dattoma V. A brief review and advances of thermographic image-processing methods for irt inspection: a case of study on gfrp plate. Exp Tech 2021;45(4):429–43.
[41] Dattoma V, Nobile R, Panella F, Saponaro A. Ndt thermographic techniques on cfrp structural components for aeronautical application. Procedia Struct Integr 2018;8:452–61.
[42] Dattoma V, Panella FW, Pirinu A, Saponaro A. Ultrasonic and thermographic studies for cfrp inspections with real and simulated defects. Mater Today: Proc 2021;34:224–34.
[43] Usamentiaga R, Venegas P, Guerediaga J, Vega L, López I. Automatic detection of impact damage in carbon fiber composites using active thermography. Infrared Phys Technol 2013;58:36–46.
[44] Sfarra S, Ibarra-Castanedo C, Theodorakeas P, Avdelidis NP, Perilli S, Zhang H, Nardi I, Koui M, Maldague XP. Evaluation of the state of conservation of mosaics: Simulations and thermographic signal processing. Int J Therm Sci 2017;117:287–315.
[45] Maldague X, Marinetti S. Pulse phase infrared thermography. J Appl Phys 1996;79(5):2694–8.
[46] Lopez F, Ibarra-Castanedo C, de Paulo Nicolau V, Maldague X. Optimization of pulsed thermography inspection by partial least-squares regression. NDT & E Int 2014;66:128–38.
[47] Wu S, Gao B, Woo WL, Yu Y, Yang Y. Defect super-resolution algorithm based on infrared thermal imaging physical kernel. NDT & E Int 2025;154:103368.

[48] Kang Y, Liu L, Gao B, Li J, Zeng Y, Woo WL. Automated thermography cognitive sensing-feedback inspection for large irregular sample. IEEE Trans Instrum Meas 2024.
[49] Zhang X, Gao B, Wu T, Woo WL, Fan J, Zhan S. Differentiate tensor low rank soft decomposition in thermography defect detection. NDT & E Int 2023;139:102902.
[50] Ahmed J, Gao B, Woo WL, Zhu Y. Ensemble joint sparse low-rank matrix decomposition for thermography diagnosis system. IEEE Trans Ind Electron 2020;68(3):2648–58.
[51] Vavilov VP. In: Dynamic thermal tomography: perspective field of thermal ndt, in thermosense XII: an international conference on thermal sensing and imaging diagnostic applications, vol. 1313, SPIE; 1990, p. 178–82.
[52] Vavilov VP, Grinzato E, Bison PG, Marinetti S, Bressan C. Thermal characterization and tomography of carbon fiber reinforced plastics using individual identification technique. Mater Eval 1996;54(5).
[53] Usamentiaga R, Sfarra S, Ibarra-Castanedo C, Zhang H, Maldague X. Multi-scale contrast-to-noise ratio (MS-CNR): a novel metric for quantitative defect characterization without manual region specification. Nondestruct Test Eval 2025.
[54] Lindeberg T. Image matching using generalized scale-space interest points. J Math Imaging Vision 2015;52:3–36.
[55] Cheng C, Na R, Shen Z. Thermographic laplacian-pyramid filtering to enhance delamination detection in concrete structure. Infrared Phys Technol 2019;97:162–76.
[56] Kong H, Akakin HC, Sarma SE. A generalized laplacian of gaussian filter for blob detection and its applications. IEEE Trans Cybern 2013;43(6):1719–33.
[57] Erazo-Aux J, Loaiza-Correa H, Restrepo-Giron AD, Ibarra-Castanedo C, Maldague X. Thermal imaging dataset from composite material academic samples inspected by pulsed thermography. Data Brief 2020;32:106313.
[58] Usamentiaga R, Garcia D, Ibarra-Castanedo C, Maldague X. Highly accurate geometric calibration for infrared cameras using inexpensive calibration targets. Measurement 2017;112:105–16.